Experimental verification of the nonadiabatic effect in strong-field ionization with elliptical polarization

Min Li,[1,2] Ming-Ming Liu,[1] Ji-Wei Geng,[1] Meng Han,[1] Xufei Sun,[1] Yun Shao,[1] Yongkai Deng,[1] Chengyin Wu,[1,3] Liang-You Peng,[1,3] Qihuang Gong,[1,3] and Yunquan Liu[1,3,*]

[1]*Department of Physics and State Key Laboratory for Mesoscopic Physics, Peking University, Beijing 100871, People's Republic of China*

[2]*School of Physics and Wuhan National Laboratory for Optoelectronics, Huazhong University of Science and Technology, Wuhan 430074, People's Republic of China*

[3]*Collaborative Innovation Center of Quantum Matter, Beijing 100871, People's Republic of China*

(Received 16 August 2016; published 31 May 2017; corrected 2 June 2017)

We perform high-resolution measurement of ellipticity-resolved momentum distributions from tunneling ionization of atoms along the major and minor axes in strong elliptically polarized fields, respectively. With developing a subcycle nonadiabatic strong-field tunneling theory for arbitrary laser polarization, we show that the electron initial conditions for positions and momenta after the tunneling are nonadiabatically intertwined with the instantaneous laser field. We extract the transverse and longitudinal momentum distributions at the tunnel exit with respect to the field ellipticity. We calibrate the laser intensity with *ab initio* calculation by solving the time-dependent Schrödinger equation. The nonadiabatic effects are confirmed experimentally and theoretically. Disentangling the effect of the long-range Coulomb potential from the laser field, we have further demonstrated that the momentum-time structure of the tunneling wave packet in strong laser fields can be approximatively imaged when treating the Coulomb effect perturbatively.

DOI: 10.1103/PhysRevA.95.053425

I. INTRODUCTION

Electron tunneling is one of the critical processes when atoms and molecules are exposed to strong laser fields [1]. In low-frequency fields, tunneling is usually treated as if the electron penetrates a static barrier created by the binding potential and the instantaneous electric field in adiabatic approximation. This picture is traditionally described by the Ammosov-Delone-Krainov (ADK) theory [2,3]. Increasing the laser frequency, i.e., when the Keldysh parameter $\gamma \sim 1$ ($\gamma = \sqrt{I_p/2U_p}$, I_p is the ionization potential, U_p the ponderomotive potential, $U_p = E_0^2/4\omega^2$, E_0 the field amplitude, and ω the field frequency; atomic units are used throughout unless otherwise specified), the tunneling barrier would be time dependent and nonadiabatic effects are expected to be important in the tunneling process [4]. Recently, there have been considerable theoretical works which have predicted the existence of nonadiabatic effects in the strong-field tunneling process [5–13]. However, the experimental test of nonadiabaticity is particularly complicated, and it has been shown that nonadiabatic effects are less significant [14,15]. A controversial, even conflicting conclusion between the theory and experiment has been made.

In reality, both steps, electron tunneling and subsequent motion in the laser and Coulomb fields, are intrinsically intertwined, preventing an unambiguous investigation of the isolated tunneling process itself [13]. Nonetheless, some modern powerful techniques, such as the attoclock [16], principally rely on a well-defined relation between the measured electron momentum and the laser phase at the moment of electron emission. Using the angular streaking method, the position of the tunnel exit was revealed in near-circularly polarized laser fields within the tunnel ionization in parabolic coordinates with induced dipole and Stark shift (TIPIS) model [17]. The reconstructed momentum distribution transverse to the instantaneous laser field direction at the tunnel exit (initial transverse momentum) in circularly polarized laser fields was shown to be larger than the prediction of the adiabatic tunneling theory [14]. The discrepancy was improved by consideration of the effect of the preexponential factors [18]. As to the momentum parallel to the instantaneous laser field at the tunnel exit (initial longitudinal momentum), a common assumption widely used is to set it to zero in adiabatic theory [3]. Through high-harmonic generation by orthogonally polarized two-color laser fields, a nonzero initial longitudinal momentum offset at the tunnel exit was revealed [19]. The width of the initial longitudinal momentum spread is still controversial [20,21]. In all experimental cases, only one physical quantity was measured and the other physical quantities were regarded to vary independently. The position of the tunnel exit and momentum at the tunnel exit cannot be determined to arbitrarily high accuracy because of Heisenberg's uncertainty principle. Hence it is necessary to describe the tunneling current consistently and to solve the controversy between the theory and the experiment.

In this paper, we perform high-resolution experimental measurements of the ellipticity-resolved momentum distributions from tunneling ionization of atoms along the minor and the major axes of the laser ellipse, respectively. Then we present a subcycle nonadiabatic tunneling theory based on the strong-field approximation (SFA) in terms of quantum orbits [22,23]. The electron initial conditions are shown to be nonadiabatically coupled with each other at each electron emission time. By investigating the ellipticity-resolved photoelectron momentum distributions, we show that the nonadiabaticities lead to very different initial momentum distributions compared to the adiabatic case. We further single

*Yunquan.liu@pku.edu.cn

 ©2017 American Physical Society

out the effect of the long-range ionic potential and demonstrate that the momentum-time structure of the tunneling wave packet can be reconstructed using strong elliptically polarized laser fields.

II. EXPERIMENTAL METHOD

Experimentally, linearly polarized laser pulses (25 fs, 790 nm, 3 kHz) were produced from a multipass amplifier Ti:sapphire laser system. The momentum spectra of ions were measured by a cold target recoil-ion momentum spectrometer (COLTRIMS) setup [24] applied with a static electric field ($\sim$3 V/cm). When rotating the laser polarization, it is very difficult to measure the ellipticity-dependent momentum distribution for electrons. Thus we turn to measuring the ellipticity-dependent momentum distribution of ions because the momenta of electrons and ions are conserved for single ionization. For the input linearly polarized laser pulses, the ellipticity was controlled by rotating the relative orientation of the fast axis of a half-wave plate, which was put in front of a quarter-wave plate before the vacuum chamber. The ellipticity-dependent momentum vectors along the major axis and the minor axis in the polarization plane can be measured, respectively, along the time-of-flight (TOF) direction where we have the best momentum resolution for ions.

As known, the calibration of the laser intensity in the strong-field community is a hard task and is always model dependent. In this work, we calibrated the laser intensity with an *ab initio* method, i.e., solving the time-dependent Schrödinger equation, which is independent of particular models (see the Appendix). The effective intensity of the laser pulse was calibrated to be $\sim 1.2 \times 10^{14}$ W/cm^2 for the experiment. Using the calibrated effective intensity $I_{\rm eff}$, one obtains the peak intensity I_0 with the relationship $I_{\rm eff} = \frac{1}{N}\int_0^{I_0} I \frac{dN}{dI} dI$, where N is the relative number of photoelectron, $\frac{dN}{dI} \propto W(I)\frac{dV}{dI}$, $W(I)$ is the ionization probability, and $\frac{dV}{dI} \propto \frac{1}{I^{5/2}}(I_0 + 2I)(I_0 - I)^{1/2}$ is the volume in the laser focus. The peak intensity is $\sim 1.52 \times 10^{14}$ W/cm^2 when the effective intensity is 1.2×10^{14} W/cm^2.

III. THEORETICAL MODEL

A. Adiabatic model

To test nonadiabaticity, we first calculate the ellipticity-dependent momentum distributions along the major and minor axes using the classical-trajectory Monte Carlo method within the adiabatic approximation (see [21] for more details). In this adiabatic model, the electron initial position along the laser polarization direction is derived from the Landau's effective potential theory [25]. The tunneled electrons have a Gaussian-like distribution on the transverse momentum perpendicular to the instantaneous laser field and zero longitudinal momentum along the instantaneous laser field. Each electron trajectory is weighted by the ADK ionization rate [4,5]. After tunneling the electron evolution in the combined laser field and Coulomb field is solved via the classical Newtonian equation; i.e., $\ddot{\mathbf{r}} = -\mathbf{r}/r^3 - \mathbf{F}(t)$ [$\mathbf{r}$ is the distance from the electron to the nucleus and $\mathbf{F}(t)$ is the electric field of the laser pulse]. After the momenta and the positions of the electrons are recorded at the end of the laser field, the three-dimensional asymptotic momenta are obtained.

B. Nonadiabatic model

To overcome the controversial situation between the adiabatic theory and measurement, we have further developed a subcycle nonadiabatic theory for arbitrary laser polarization. A laser field with arbitrary ellipticity ε is given by the vector potential and the electric field, respectively,

$$\begin{aligned} \mathbf{A}(t) &= -\frac{F_0}{\omega}\sin(\omega t)\mathbf{z} + \varepsilon\frac{F_0}{\omega}\cos(\omega t)\mathbf{x}, \\ \mathbf{F}(t) &= F_0\cos(\omega t)\mathbf{z} + \varepsilon F_0 \sin(\omega t)\mathbf{x}, \end{aligned} \tag{1}$$

where $\mathbf{z}$ is the major axis and $\mathbf{x}$ is the minor axis. Based on the strong-field approximation involving the quantum orbits (see, e.g., Refs. [22,23,26,27]), the transition rate from the ground state to a continuum state can be calculated with exponential accuracy,

$$W = \exp\{-2\,\mathrm{Im}S\}, \tag{2}$$

$$S = \int_{t_s}^{t_0} dt \left\{ \frac{1}{2}[\mathbf{P} + \mathbf{A}(t)]^2 + I_p \right\}, \tag{3}$$

where t_0 is a point on the real axis of t (the ionization time), and t_s is the complex transition point. Here $\mathbf{P}$ is the drift momentum (the conserved canonical momentum), which is a real value. Thus the complex transition point t_s should satisfy the saddle-point equation [26,27],

$$\tfrac{1}{2}[\mathbf{P} + \mathbf{A}(t_s)]^2 + I_p = 0. \tag{4}$$

We assume $t_s = t_0 + \mathrm{i}t_i$, where t_0 is the ionization time and t_i is the so-called tunneling time [1]. Using the laser field of Eq. (1), we have

$$\begin{aligned} &\tfrac{1}{2}(P_z - F_0/\omega \sin\omega t_0 \cosh\omega t_i - i F_0/\omega \cos\omega t_0 \sinh\omega t_i)^2 \\ &\quad + \tfrac{1}{2}(P_x + \varepsilon F_0/\omega \cos\omega t_0 \cosh\omega t_i \\ &\quad - i\varepsilon F_0/\omega \sin\omega t_0 \sinh\omega t_i)^2 + \tfrac{1}{2}P_y^2 + I_p = 0. \end{aligned} \tag{5}$$

Using the relationship between the initial momentum $\mathbf{v} = (v_x, v_y, v_z)$ and the conserved canonical momentum $\mathbf{P}$,

$$\begin{aligned} P_z &= v_z + F_0 \sin(\omega t_0)/\omega \\ P_x &= v_x - \varepsilon F_0 \cos(\omega t_0)/\omega \\ P_y &= v_y, \end{aligned} \tag{6}$$

where v_x,v_y, and v_z are the initial momentum at the tunnel exit point along the x, y, and z directions, respectively. At an instantaneous laser phase, the initial longitudinal momentum v_p and initial transverse momentum $v_\perp$ with respect to the instantaneous laser polarization direction at the tunnel exit should satisfy

$$\begin{aligned} v_z &= v_p\cos\beta - v_\perp \sin\beta \\ v_x &= v_p \sin\beta + v_\perp \cos\beta, \end{aligned} \tag{7}$$

where $\beta = \tan^{-1}(\varepsilon \tan\omega t_0)$ is the angle between the instantaneous laser polarization direction and the $\mathbf{z}$ axis. v_p is positive when the direction is the same as that of the instantaneous laser

field. Thus Eq. (6) can be rewritten as

$$\begin{aligned} P_z &= \mathrm{sgn}(F_z)[v_p/\sqrt{1+\varepsilon^2\tan^2\omega t_0} - v_\perp \varepsilon \tan\omega t_0/\sqrt{1+\varepsilon^2\tan^2\omega t_0}] + F_0 \sin\omega t_0/\omega \\ P_x &= \mathrm{sgn}(F_z)[v_p \varepsilon \tan\omega t_0/\sqrt{1+\varepsilon^2\tan^2\omega t_0} + v_\perp/\sqrt{1+\varepsilon^2\tan^2\omega t_0}] - \varepsilon F_0 \cos\omega t_0/\omega \\ P_y &= v_y, \end{aligned} \tag{8}$$

where $\mathrm{sgn}(F_z) = 1$ for $F_z \geqslant 0$, and $\mathrm{sgn}(F_z) = -1$ for $F_z < 0$. Substituting Eq. (8) into Eq. (5), one obtains

$$\cosh\omega t_i = \begin{cases} \frac{1}{a^4-\varepsilon^2}\left[\varepsilon\left(a\frac{\omega}{F_0}v_\perp - \varepsilon\right) \pm a^2\sqrt{\left(a\frac{\omega}{F_0}v_\perp - \varepsilon\right)^2 + (a^4-\varepsilon^2)(1+{\gamma_{\mathrm{eff}}}^2/a^2)}\right], & a^2 \neq |\varepsilon| \\ \frac{1}{2}\left(1 - \frac{a\omega}{\varepsilon F_0}v_\perp\right) + \frac{a^2}{\varepsilon^2}(1+{\gamma_{\mathrm{eff}}}^2/a^2)/\left[2\left(1-\frac{a\omega}{\varepsilon F_0}v_\perp\right)\right], & a^2 = |\varepsilon| \end{cases}, \tag{9}$$

$$v_p = \frac{(1-\varepsilon^2)F_0 \sin\omega t_0 \cos\omega t_0}{a\omega}(\cosh\omega t_i - 1), \tag{10}$$

where $a = |F(t_0)|/F_0 = \sqrt{\cos^2\omega t_0 + \varepsilon^2 \sin^2\omega t_0}$ is the normalized instantaneous laser field and $\gamma_{\mathrm{eff}} = \omega\sqrt{2(I_p + {v_y}^2/2)}/F_0$ is the effective Keldysh parameter [28]. Both the tunneling time t_i and the initial longitudinal momentum v_p are functions of the ionization time t_0 and the initial transverse momentum $v_\perp$, v_y.

To calculate the ionization probability, one needs to calculate the classical action under the barrier, which is expressed as

$$S = -\int_{t_s}^{t_0} dt \left\{\frac{1}{2}[\mathbf{P} + \mathbf{A}(t)]^2 + I_p\right\}. \tag{11}$$

Using the laser field of Eq. (1), then

$$\begin{aligned} S = i\left[\frac{P^2}{2} + I_p + U_p\right]t_i - P_z\frac{F_0}{\omega^2}(\cos\omega t_0 - \cos\omega t_s) \\ - P_x\frac{\varepsilon F_0}{\omega^2}(\sin\omega t_0 - \sin\omega t_s) \\ + \frac{(1-\varepsilon^2)F_0^2}{8\omega^3}(\sin 2\omega t_0 - \sin 2\omega t_s), \end{aligned} \tag{12}$$

where $U_p = \frac{(1+\varepsilon^2)F_0^2}{4\omega^2}$ is the ponderomotive energy. The real part of Eq. (12) is related to a phase shift for the trajectory under the barrier [27], while the imaginary part is related to the ionization probability. Thus the ionization probability is expressed as

$$\begin{aligned} W_s &= \exp(-2\,\mathrm{Im}S) \\ &= \exp\left[-2\left(\frac{P^2}{2} + I_p + U_p\right)t_i + 2P_z\frac{F_0}{\omega^2}\sin\omega t_0 \sinh\omega t_i \right. \\ &\quad - 2P_x\frac{\varepsilon F_0}{\omega^2}\cos\omega t_0 \sinh\omega t_i \\ &\quad \left. + \frac{(1-\varepsilon^2)F_0^2}{4\omega^3}\cos 2\omega t_0 \sinh 2\omega t_i\right]. \end{aligned} \tag{13}$$

The instantaneous tunneling time v and the asymptotic momentum $P = \sqrt{P_x^2 + P_y^2 + P_z^2}$ are given by Eq. (8). Substituting Eq. (8) into Eq. (13), the instantaneous ionization rate and the initial momentum distributions are obtained, which makes no assumption on the electron momentum at the tunnel exit.

The position of the tunnel exit point is related to the subbarrier trajectory [27]:

$$\mathbf{r}_0(t) = \int_{t_s}^{t} dt'[\mathbf{P} + \mathbf{A}(t')]. \tag{14}$$

Thus $\mathbf{r}_0(t)$ is expressed as

$$\begin{aligned} z(t) &= P_z(t-t_s) + \frac{F_0}{\omega^2}(\cos\omega t - \cos\omega t_s) \\ x(t) &= P_x(t-t_s) + \frac{\varepsilon F_0}{\omega^2}(\sin\omega t - \sin\omega t_s) \\ y(t) &= P_y(t-t_s). \end{aligned} \tag{15}$$

The tunnel exit point is the real part of the position when $\tau = 0$; thus it is written as

$$\begin{aligned} \mathrm{Re}z(t_0) &= \frac{F_0}{\omega^2}\cos\omega t_0(1-\cosh\omega t_i) \\ \mathrm{Re}x(t_0) &= \frac{\varepsilon F_0}{\omega^2}\sin\omega t_0(1-\cosh\omega t_i) \\ \mathrm{Re}y(t_0) &= 0. \end{aligned} \tag{16}$$

From Eq. (16), one can see that the tunnel exit point is along the instantaneous laser field direction in the nonadiabatic model.

We further consider the effect of the under-the-barrier Coulomb potential on the ionization probability and the initial momentum distributions. The Coulomb effect can be included by [29]

$$S^C = -\int_{t_s}^{t_0} dt\, V[r_0(t)], \tag{17}$$

where $r_0(t)$ is the unperturbed trajectory in the laser field given by Eq. (15). Because the Coulomb potential is divergent at $r = 0 (t = t_s)$, we use a matching procedure the same as in Ref. [29]. Therefore Eq. (17) can be transformed into

$$S^C = -i\frac{Z}{\kappa}\ln\kappa r_1 - i\int_{t_1}^{0} dt\, V[r_0(t)], \tag{18}$$

where t_1 (and the corresponding position r_1) is the matching point, $\kappa = \sqrt{2I_p}$, and Z is the nuclear charge. The first term in Eq. (18) comes from the asymptotic wave function of the

field-free atom, which can be expressed as

$$-i\frac{Z}{\kappa}\ln\kappa r_1 = i\frac{Z}{\kappa}\int_{t_i-\frac{1}{\kappa^2}}^{t_1}\frac{d\tau}{t_i-\tau} = i\frac{Z}{\kappa}\int_0^{t_1}\frac{d\tau}{t_i-\tau} - i\frac{Z}{\kappa}\ln\kappa^2 t_i. \quad (19)$$

Thus Eq. (18) can be rewritten as

$$S^C = -i\frac{Z}{\kappa}\ln\kappa^2 t_i - i\frac{Z}{\kappa}\int_0^{t_i} d\tau\left[\frac{\kappa}{r_0(\tau)} - \frac{1}{t_i-\tau}\right]. \quad (20)$$

We have taken in Eq. (20) a limit as $t_1 \to t_i$; therefore the dependence of S^C on the matching point has dropped out. Generally, $r_0(\tau)$ and S^C are complex. We focus on the imaginary part of S^C, which is responsible for the Coulomb-corrected ionization rate. Thus

$$\mathrm{Im}S^C = -\frac{Z}{\kappa}\ln\kappa^2 t_i - \frac{Z}{\kappa}\int_0^{t_i} d\tau\left(\frac{\kappa|r_1|}{{r_1}^2+{r_2}^2} - \frac{1}{t_i-\tau}\right), \quad (21)$$

where r_1 and r_2 are the real and imaginary part of $r_0(\tau)$, respectively. As a result, the Coulomb-corrected ionization probability is

$$W_L = \left[\frac{2(2I_p)^{3/2}}{F_0}C(t_0,v_\perp,v_y)\right]^{\frac{2Z}{\kappa}} W_S, \quad (22)$$

where W_S is the ionization probability of Eq. (13), and

$$C(t_0,v_\perp,v_y) = \frac{\phi_i}{2\gamma}\exp\left\{\int_0^{\phi_i} d\phi\left[\frac{\kappa|r_1|}{\omega\left(r_1^2+r_2^2\right)} - \frac{1}{\phi_i-\phi}\right]\right\}, \quad (23)$$

with $\phi_i = \omega t_i$. In this part, we have derived the subcycle-resolved nonadiabatic tunneling theory.

From Eqs. (9) and (10), one can see that the ionization time t_i and the initial momentum at the tunnel exit are coupled in the laser field because of nonadiabatic effects. Here, the distribution of the initial longitudinal momentum and the position of the tunnel exit are derived self-consistently. One should note that the nonadiabatic tunneling coordinates, i.e., the tunnel exit and the initial momentum distribution, will converge in the adiabatic theory [2,3,26] when the Keldysh parameter approaches zero.

Starting with the initial nonadiabatic coordinates derived above, one can calculate photoelectron momentum distributions on the detector by numerically solving the classical Newtonian equation with consideration of the Coulomb effect.

IV. RESULTS AND DISCUSSIONS

We have measured the ellipticity-dependent momentum distribution of rare gases, i.e., Ne, Ar, and Kr atoms. Here, we present the typical results of Ar as an example. In Fig. 1, we show the measured ellipticity-dependent TOF spectra of Ar^+ ions along the minor axis (the red rectangle) and along the major axis (the blue rectangle). In order to reveal the width of ellipticity-dependent momentum distributions, we normalize the momentum spectra using the maximum yields at each ellipticity value, as seen in Figs. 2(a) and 2(d).

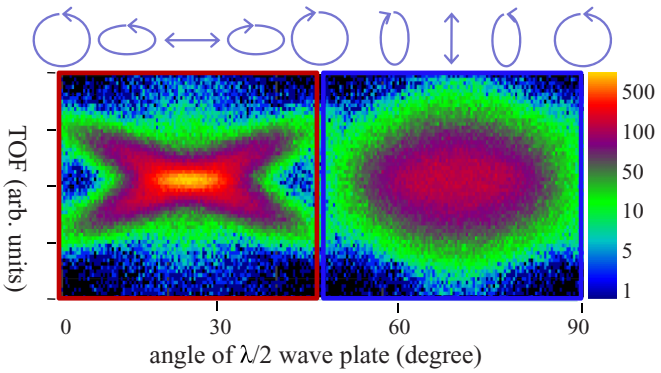

FIG. 1. The measured ellipticity-dependent TOF spectra of Ar^+ ions along the minor axis (framed red, left) and along the major axis (framed blue, right).

Generally, the ellipticity-resolved momentum distribution along the minor axis show a "cross" structure. The ellipticity-resolved momentum distribution along the major axis reveals a "bridge" structure. Note that the ponderomotive energy is fixed in the experiment. The ellipticity-resolved measurement allows us to calibrate the laser intensity with high resolution (see the Appendix).

Using the calibrated effective laser intensity, i.e., $1.2\times10^{14}\,\mathrm{W/cm^2}$, we obtain the ellipticity-resolved final momentum distributions along the major and minor axes of the laser ellipse, respectively, within the adiabatic model as shown in Figs. 2(c) and 2(f). Compared with the experimental data [Figs. 2(a) and 2(d)], one can find that both the peaks of the momentum p_x and the width of momentum p_z using the adiabaticity-based simulation are underestimated by ~17% and 20%, respectively. In fact, the simulated momentum distributions by the adiabatic model reveals a smaller ring structure as compared with the TDSE result in circularly polarized laser fields [30].

We have also simulated the ellipticity-dependent momentum distributions along the minor and major axes using the nonadiabatic model, as seen in Figs. 2(b) and 2(e), respectively. The nonadiabatic simulation agrees with the measured spectra much better than that of the adiabatic model.

To further validate the nonadiabatic model, we show the direct comparison of the simulated final momentum distributions with the *ab initio* TDSE results using the same laser parameters in Fig. 3. In order to lower the influence of electron interferences on the momentum distribution from the TDSE, we have considered the intensity averaging effect in the focal volume. We calculate the photoelectron momentum spectra for a series of laser intensities with the effective intensity of $1.2\times10^{14}\,\mathrm{W/cm^2}$. Then the momentum spectrum of each intensity is weighted by the volume in the laser focus, i.e., $\frac{dV}{dI}\propto\frac{1}{I^{5/2}}(I_0+2I)(I_0-I)^{1/2}$, where I_0 is the peak laser intensity. As seen in Fig. 3, the nonadiabatic simulation agrees much better with the TDSE result for $\varepsilon = 0.6$, as compared with the adiabatic simulation. The size of the momentum distribution from the adiabatic simulation is smaller than that of the TDSE result and the nonadiabatic simulation. The most probable momentum along the radial direction of the adiabatic simulation is also smaller than that by the TDSE and the

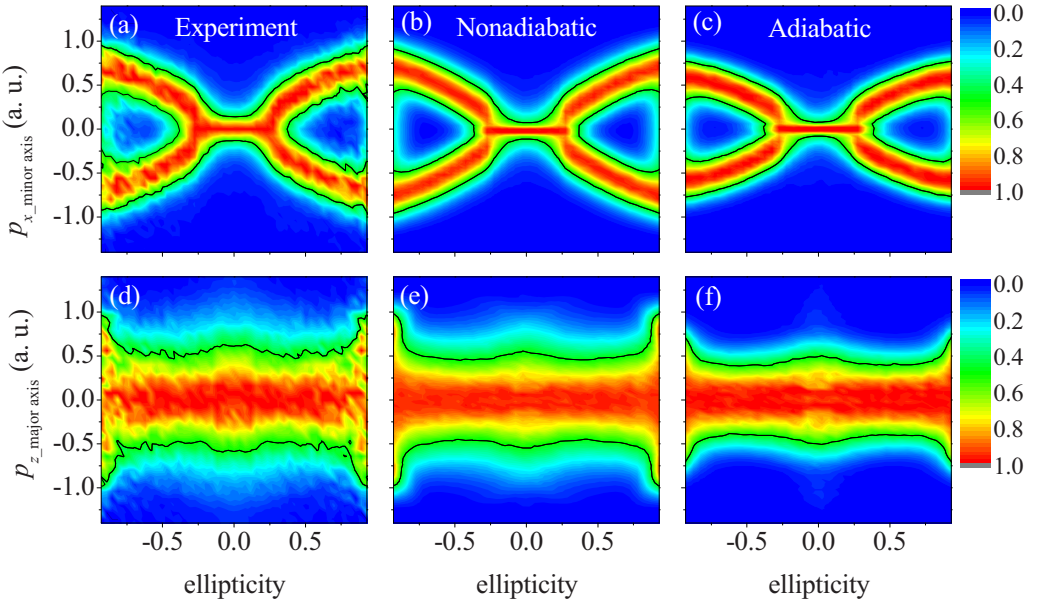

FIG. 2. The ellipticity dependence of final momentum distribution along the minor axis (top row) and the major axis (bottom row) at the effective intensity 1.2×10^{14} W/cm^2 of Ar for the measurement (a), (d), nonadiabatic simulation (b,e), and adiabatic simulation (c), (f). The counts of the plots are normalized for each ellipticity value. The black curves indicate where the ion yield dropped to half of the maximum.

nonadiabatic simulation. Moreover, an evident tilt angle can be observed in all the momentum spectra, which is a result of the Coulomb potential effect [21]. Note that the propagation of the electron wave packet after the tunneling is the same for the adiabatic and nonadiabatic simulations. The only difference between the nonadiabatic and the adiabatic simulations is that the initial momentum-temporal distribution of the tunneling wave packet is given by the nonadiabatic model in Fig. 3(b) while it is given by the ADK theory in Fig. 3(c). Thus nonadiabaticities have left a pronounced imprint on the momentum-temporal distribution of the tunneling electron wave packet.

In light of the good agreement between the nonadiabatic simulation with the measurement (Fig. 2) and the TDSE result (Fig. 3), we have calculated the ellipticity-dependent half-cycle averaged initial transverse and longitudinal momentum distribution predicted at the intensity of 1.2×10^{14} W/cm^2 (800 nm) using the nonadiabatic theory [Eq. (22)], as shown in Figs. 4(a) and 4(b), respectively. The initial transverse momentum at half maximum is given by the dark gray lines in Fig. 4(a). In the elliptically polarized laser field, the initial transverse momentum distribution is not centered at zero due to the rotation of the laser electric field, which is in contrast with the ADK theory [3]. Increasing the field ellipticity, the most probable initial transverse momentum also increases. This agrees with the result predicted by the Perelomov-Popov-Terent'ev (PPT) theory [5], as shown by the white dashed curve in Fig. 4(a). The width of the distribution slightly decreases with the increase of the field ellipticity.

More interestingly, from this model, we can further obtain the half-cycle averaged initial longitudinal momentum distribution at the tunnel exit with respect to the ellipticity, as shown in Fig. 4(b). Different from the transverse momentum at the tunnel exit, the longitudinal momentum reveals much narrower distribution and its width is around 0.2 a.u. It is insensitively dependent on the ellipticity when $\varepsilon < 0.8$ and will decrease to zero for a circularly polarized laser field. The calculated longitudinal momentum distributions at the tunnel exit agree with the experimental calibration [21,31], in which an arbitrary longitudinal momentum distribution is put into the

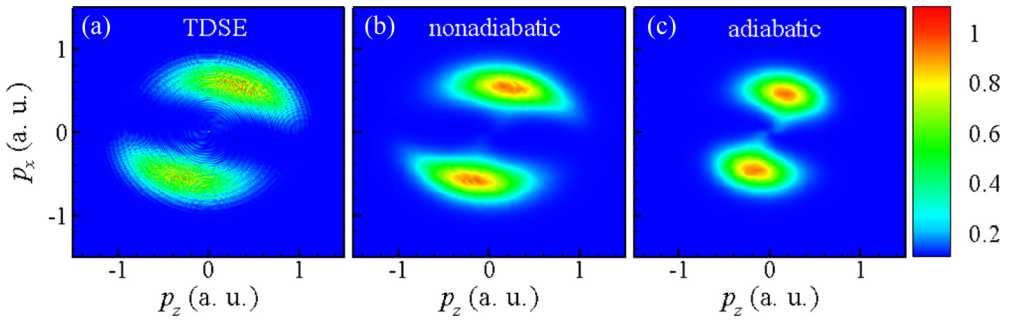

FIG. 3. The simulated photoelectron momentum distributions from (a) the TDSE result, (b) the nonadiabatic model, and (c) the adiabatic model. The Coulomb potential effect and the focal volume effect are included in the simulations. The effective laser intensity is 1.2×10^{14} W/cm^2 and the ellipticity is 0.6.

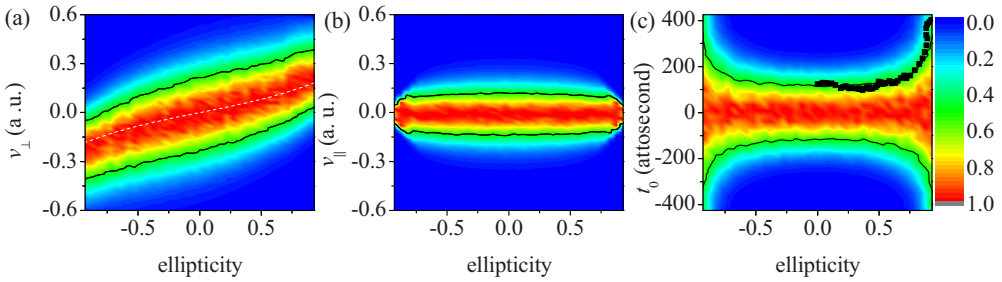

FIG. 4. (a) Theoretical prediction of the half-cycle averaged initial transverse momentum distribution. The white dashed line indicates the center of the initial transverse momentum distribution predicted in Ref. [5]. (b) Theoretical prediction of the half-cycle averaged initial longitudinal momentum distribution. (c) Theoretical prediction of the ionization probability as a function of the ionization time. The black solid lines indicate where the yield is the half maximum. The experimentally extracted ionization time at half maximum is shown with black squares in (c).

ADK model. As known, it was assumed to be zero in the ADK model.

Both the initial transverse and longitudinal momentum distributions at the tunnel exit have important effects on the final momentum distributions on the "detector." In order to experimentally extract the initial tunneling coordinates at the tunnel exit, one should consider the Coulomb effect on photoelectron momentum distributions, but it has been usually ignored in attosecond angular streaking experiments. In the nonadiabatic picture, the initial transverse momentum and longitudinal momentum distributions, and the position of the tunnel exit are coupled with the rotating instantaneous laser field. The electrons with an initial transverse momentum and longitudinal momentum will be streaked to a certain final momentum along the minor and major axes in the laboratory frame, respectively. Since the electrons are most probably released at the field maximum (along the major axis of an elliptically polarized field), the final momentum along the minor axis and major axis will approximately be linear with the initial transverse momentum and the ionization time, respectively. As a result, the ellipticity-dependent momentum-temporal structure of the tunneling wave packet at the tunnel exit could be directly mapped onto the final momentum distribution along the major and minor axes if the Coulomb effect can be properly estimated.

The center of the final momentum along the minor axis (with the maximum ionization probability) in an elliptically polarized field can be predicted by the PPT theory [4], i.e., $p_0 = \varepsilon F_0/\omega \sinh(\omega\tau_0)/(\omega\tau_0)$ where τ_0 is the tunneling time for the most probable trajectory, as shown by the green solid line in Fig. 5(a). The measured and simulated centers of the final momenta along the minor axis with respect to the ellipticity are shown in Fig. 5(a) by the black squares and the red dots, respectively. Due to the Coulomb focusing effect, the measured and simulated centers of the final momentum along the minor axis are smaller than the prediction by PPT theory.

If ignoring the effect of the Coulomb potential, the momentum along the minor axis at half maximum will shift up parallel with the field momentum $\varepsilon F_0/\omega$, as shown by the green triangles in Fig. 5(b). Experimentally, the measured final momentum along the minor axis at half maximum is also shown in Fig. 5(b). One clearly find that the Coulomb potential has two important effects on the final momentum: (i) reducing the final momentum along the minor axis significantly because of strong Coulomb focusing when the ellipticity is below 0.3, and (ii) reducing the final momentum along the minor axis by around 0.1 a. u. compared with the Coulomb-free case (the PPT case) when the ellipticity is larger than 0.3.

Compared with Figs. 5(a) and 5(b), one finds that the Coulomb potential leads to a shift of around 0.1 a.u. for the momentum distributions along the minor axis as a whole when the ellipticity is larger than 0.3. Therefore, the full width at half maximum (FWHM) of the final momentum along the minor axis [the gray arrow in Fig. 5(b)] directly reflects the width of the initial transverse momentum when $\varepsilon > 0.3$.

With treating the Coulomb potential as a perturbation when $\varepsilon > 0.3$, the initial transverse momentum at the tunnel exit can be directly related to the final momentum p_x along the minor

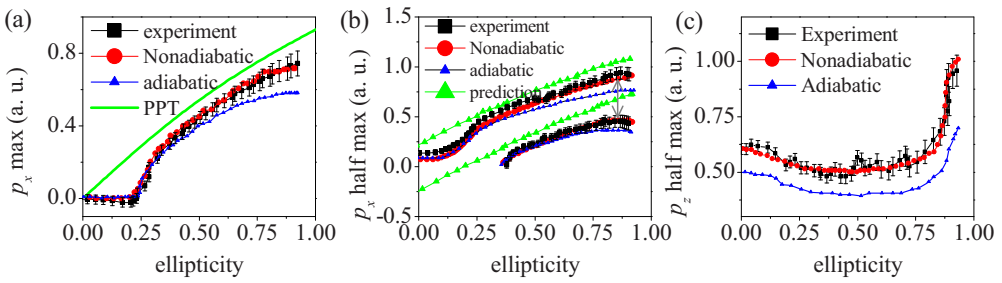

FIG. 5. (a) The peak of the final momentum p_x with respect to the laser ellipticity. The black curves with squares and the red curves with dots are experimental and simulated results, respectively. The green curve is the prediction of PPT theory [4]. (b) The final momentum p_x at half maximum yield. The green curve with triangles shows the initial transverse momentum shifted up by $\varepsilon F_0/\omega$. The gray arrow shows the width of the final momentum p_x at half maximum of the momentum distribution. (c) The final momentum p_z at half maximum yield.

axis by the approximate expression of $p_x = v_\perp + \varepsilon F_0/\omega + p_x^C$, where $\varepsilon F_0/\omega$ is the electron momentum obtained from the laser field when the instantaneous field is along the major axis and p_x^C is the Coulomb-corrected momentum along the minor axis [32], respectively. Since the final momentum p_x is approximately linearly dependent on the initial transverse momentum $v_\perp$, one only need measure the momentum width at half maximum to characterize the initial transverse momentum distribution of the tunneling electron wave packet with the Gaussian distribution.

In Fig. 5(c), we show the measured and simulated final momentum p_z along the major axis at half maximum with respect to the laser ellipticity. The simulation quantitatively agrees with the experiment. It is well known that the electron released at different ionization times will be streaked to specific final momentum p_z along the major axis. Therefore, the measured momentum distribution along the major axis has recorded the temporal information of the tunneling wave packet. The final momentum p_z along the major axis is related with the ionization time t_0, which is given by Eq. (8); i.e., $p_z = v_p/\sqrt{1+\varepsilon^2\tan^2\omega t_0} - v_\perp\varepsilon\tan\omega t_0/\sqrt{1+\varepsilon^2\tan^2\omega t_0} + F_0\sin\omega t_0/\omega$. Because most electrons tunnel near the field maximum of the laser pulse, ωt_0 is a small value ($\omega t_0 = 0$ is assumed to be the field maximum). Expanding p_z and v_p in a Taylor series up to the first order with respect to t_0 and $v_\perp$ [$v_p/\sqrt{1+\varepsilon^2\tan^2\omega t_0} = \frac{(1-\varepsilon^2)F_0\sin\omega t_0\cos\omega t_0}{a\omega}(\cosh\omega t_i - 1) \approx (1-\varepsilon^2)F_0 t_0(\cosh\omega\tau_0 - 1)$, $-v_\perp\varepsilon\tan\omega t_0/\sqrt{1+\varepsilon^2\tan^2\omega t_0} \approx 0$, and $\frac{F_0}{\omega}\sin(\omega t_0) \approx F_0 t_0$], we can obtain $v_p = k_0 F_0 t_0$ and $p_z = (1+k_0)F_0 t_0$, where $k_0 = (1-\varepsilon^2)(\cosh\omega\tau_0 - 1)$ is related to the effect of the initial longitudinal momentum (τ_0 is the tunneling time in the PPT theory). Considering the Coulomb-corrected effect, one obtains $p_z = (1+k_0)F_0 t_0 + p_z^C$, where p_z^C is the Coulomb-corrected momentum along the major axis [32]. In this relation, we have included the effect of the initial longitudinal momentum.

With the linear relation between p_z and t_0, one can relate the final momentum along the major axis to the temporal distribution of the tunneling wave packet. As shown in Fig. 4(c), the reconstructed width of the tunneling wave packet (black squares) agrees well with the prediction of the nonadiabatic model (solid curve). The temporal width (FWHM) of the electron tunneling current increases from ~250 as for $\varepsilon = 0$ to ~600 as for $\varepsilon = 0.8$. When the ellipticity is larger than 0.8, the temporal width of the subcycle tunneling wave packet increases rapidly.

V. CONCLUSIONS

In summary, we have measured high-resolution ellipticity-resolved momentum distributions in strong elliptically polarized laser fields. Developing a subcycle nonadiabatic tunneling theory, we have verified the importance of nonadiabatic effects for strong-field tunneling ionization. We show that the initial momenta at the tunnel exit are intertwined at each electron emission time with respect to the laser field. Both the subcycle tunneling coordinates at the tunnel exit and the Coulomb potential are crucial in the nonadiabatic picture. We show that the momentum-time structure of the tunneling wave packet can be approximatively retrieved from the final momentum along the major and minor axes of the laser field if considering the Coulomb interaction as a perturbation. This study has significant implications for any tunneling-triggered phenomena, such as laser-induced diffraction, photoelectron holography, and molecular orbital imaging using strong laser fields.

ACKNOWLEDGMENTS

We thank Dieter Bauer and Wilhelm Becker for the constructive comments. This work is supported by 973 program (Grant No. 2013CB922403) and NSFC (Grants No. 11134002, No. 11134001, and No. 11674116).

APPENDIX: CALIBRATION OF THE EFFECTIVE LASER INTENSITY

We calibrate the laser intensity by solving the three-dimensional time-dependent Schrödinger equation (TDSE), which is independent of specific model. We numerically solve the TDSE for the argon atom within single active electron (SAE) approximation in elliptically laser fields ($\varepsilon = 0.6$) by using a grid-based split-step method for a number of laser intensities. The electron final momentum is obtained by projecting the wave function onto the Coulomb continuum scattering eigenstates after the time-dependent propagation.

Since the laser intensity is fixed when rotating the field ellipse, we can calibrate the laser intensity at a certain ellipticity. As known, the momentum distributions of p_x in the laser polarization plane show a double-peak structure in elliptically polarized fields. We show the calculated peak of p_x with respect to the laser intensity at the ellipticity of 0.6 using the TDSE calculation in Fig. 6, as an example. The peak of p_x momentum distribution [see Fig. 5(a)] increases with increasing the laser intensity. At the ellipticity of 0.6, the measured peak of p_x momentum distributions is 0.53 a.u. Along this, the effective laser intensity in our experiment can be calibrated as $(1.21 \pm 0.1) \times 10^{14}$ W/cm and the peak intensity can be calibrated.

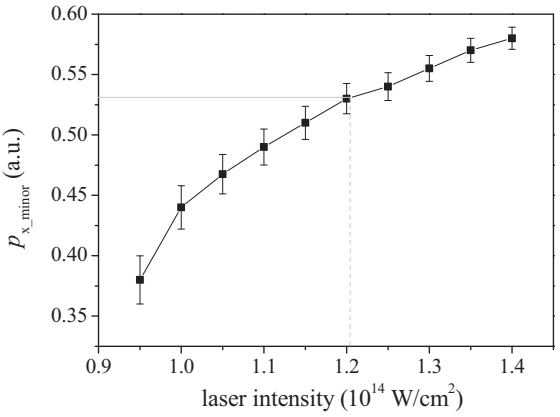

FIG. 6. The calculated peak of p_x with respect to the laser intensity at the ellipticity of 0.6 using TDSE calculation. The solid horizontal line shows the position of the measured peak at the ellipticity of 0.6.

[1] L. V. Keldysh, Sov. Phys. JETP **20**, 1307 (1965).
[2] M. V. Ammosov, N. B. Delone, and V. P. Krainov, Sov. Phys. JETP **64**, 2008 (1986).
[3] N. B. Delone and V. P. Krainov, J. Opt. Soc. Am. B **8**, 1207 (1991).
[4] A. M. Perelomov, V. S. Popov, and M. V. Terent'ev, Sov. Phys. JETP **24**, 207 (1966).
[5] V. D. Mur, S. V. Popruzhenko, and V. S. Popov, Sov. Phys. JETP **92**, 777 (2001).
[6] G. L. Yudin and M. Yu. Ivanov, Phys. Rev. A **64**, 013409 (2001).
[7] M. Yu. Ivanov, M. Spanner, and O. Smirnova, J. Mod. Opt. **52**, 165 (2005).
[8] D. I. Bondar, Phys. Rev. A **78**, 015405 (2008).
[9] I. Barth and O. Smirnova, Phys. Rev. A **84**, 063415 (2011); **87**, 013433 (2013).
[10] J. Kaushal and O. Smirnova, Phys. Rev. A **88**, 013421 (2013).
[11] I. A. Ivanov and A. S. Kheifets, Phys. Rev. A **89**, 021402(R) (2014).
[12] J.-W. Geng, L. Qin, M. Li, W. Xiong, Y. Liu, Q. Gong, and L.-Y. Peng, J. Phys. B, **47**, 204027 (2014); M. Han, M. Li, M.-M. Liu, and Y. Liu, Phys. Rev. A **95**, 023406 (2017).
[13] C. Hofmann, T. Zimmermann, A. Zielinski, and A. S. Landsman, New J. Phys. **18**, 043011 (2016).
[14] L. Arissian, C. Smeenk, F. Turner, C. Trallero, A. V. Sokolov, D. M. Villeneuve, A. Staudte, and P. B. Corkum, Phys. Rev. Lett. **105**, 133002 (2010).
[15] R. Boge, C. Cirelli, A. S. Landsman, S. Heuser, A. Ludwig, J. Maurer, M. Weger, L. Gallmann, and U. Keller, Phys. Rev. Lett. **111**, 103003 (2013).
[16] P. Eckle *et al.*, Science **322**, 1525 (2008).
[17] A. N. Pfeiffer *et al.*, Nat. Phys. **8**, 76 (2012).
[18] I. Dreissigacker and M. Lein, Chem. Phys. **414**, 69 (2013).
[19] D. Shafir *et al.*, Nature (London) **485**, 343 (2012).
[20] A. N. Pfeiffer, C. Cirelli, A. S. Landsman, M. Smolarski, D. Dimitrovski, L. B. Madsen, and U. Keller, Phys. Rev. Lett. **109**, 083002 (2012).
[21] M. Li, Y. Liu, H. Liu, Q. Ning, L. Fu, J. Liu, Y. Deng, C. Wu, L. Y. Peng, and Q. Gong, Phys. Rev. Lett. **111**, 023006 (2013); X. Sun, M. Li, J. Yu, Y. Deng, Q. Gong, and Y. Liu, Phys. Rev. A **89**, 045402 (2014).
[22] P. Salières *et al.*, Science **292**, 902 (2001).
[23] W. Becker, F. Grasbon, D. Kopold, D. B. Milošević, G. G. Paulus, and H. Walther, Adv. At., Mol. Opt. Phys. **48**, 35 (2002).
[24] J. Ullrich *et al.*, Rep. Prog. Phys. **66**, 1463 (2003).
[25] L. D. Laudau and E. M. Lifshitz, *Quantum Mechanics* (Pergamon, Oxford, UK, 1977).
[26] D. B. Milošević *et al.*, J. Phys. B **39**, R203 (2006).
[27] T. M. Yan and D. Bauer, Phys. Rev. A **86**, 053403 (2012).
[28] M. Li, J.-W. Geng, M. Han, M.-M. Liu, L.-Y. Peng, Q Gong, and Y. Liu, Phys. Rev. A **93**, 013402 (2016).
[29] A. M. Perelomov and V. S. Popov, Sov. Phys. JETP **25**, 336 (1967).
[30] N. I. Shvetsov-Shilovski, D. Dimitrovski, and L. B. Madsen, Phys. Rev. A **85**, 023428 (2012).
[31] M. Li, P. Zhang, S. Luo, Y. Zhou, Q. Zhang, P. Lan, and P. Lu, Phys. Rev. A **92**, 063404 (2015).
[32] S. P. Goreslavski, G. G. Paulus, S. V. Popruzhenko, and N. I. Shvetsov-Shilovski, Phys. Rev. Lett. **93**, 233002 (2004).